NONCODING RNA

Mechanism of siRNA production by a plant Dicer-RNA complex in dicing-competent conformation

Qian Wang[1]†, Yan Xue[2]†, Laixing Zhang[3]†, Zhenhui Zhong[2], Suhua Feng[2], Changshi Wang[1], Lifan Xiao[1], Zhenlin Yang[1], C. Jake Harris[4], Zhe Wu[1], Jixian Zhai[1], Maojun Yang[3], Sisi Li[5]*, Steven E. Jacobsen[2,6]*, Jiamu Du[1]*

In eukaryotes, small RNAs (sRNAs) play critical roles in multiple biological processes. Dicer endonucleases are a central part of sRNA biogenesis. In plants, DICER-LIKE PROTEIN 3 (DCL3) produces 24-nucleotide (nt) small interfering RNAs (siRNAs) that determine the specificity of the RNA-directed DNA methylation pathway. Here, we determined the structure of a DCL3–pre-siRNA complex in an active dicing-competent state. The 5′-phosphorylated A1 of the guide strand and the 1-nt 3′ overhang of the complementary strand are specifically recognized by a positively charged pocket and an aromatic cap, respectively. The 24-nt siRNA length dependence relies on the separation between the 5′-phosphorylated end of the guide RNA and dual cleavage sites formed by the paired ribonuclease III domains. These structural studies, complemented by functional data, provide insight into the dicing principle for Dicers in general.

Dicer family ribonuclease III (RNase III) enzymes cleave hairpin-shaped pre-microRNA (pre-miRNA) or double-stranded pre–small interfering RNA (pre-siRNA) to generate small RNAs (sRNAs) of defined length (*1*). After dicing, one sRNA strand is loaded into Argonaute (AGO) proteins, forming the active RNA-induced silencing complex (RISC), which silences target loci (*2*). Structural and biochemical analysis of *Giardia intestinalis*, human, and *Drosophila* Dicers in RNA-free or pre-dicing states have defined overall Dicer topology and function (*3*–*7*). However, the structure of Dicer in a cleavage-competent conformation has yet to be determined, limiting current understanding of the dicing mechanism.

In *Arabidopsis*, there are four DICER-LIKE PROTEINS (DCLs). Although DCL1 produces 21-nt miRNAs (*8*), DCL2, DCL3, and DCL4 produce 22-, 24-, and 21-nt siRNAs, respectively (*9*–*12*), in which DCL3 functions specifically in the plant-specific RNA-directed DNA methylation (RdDM) pathway. In RdDM, plant-specific RNA polymerase IV (Pol IV) transcribes precursor RNAs, which are converted into double-stranded RNA (dsRNA) by RNA-DEPENDENT RNA POLYMERASE 2 (RDR2) and diced by DCL3 (*13*–*17*). The 24-nt siRNA strand is loaded into AGO4, which interacts with Pol V–transcribed long noncoding RNAs and recruits DOMAINS-REARRANGED METHYLASE 2 (DRM2), facilitating DNA methylation (*18*–*21*). DCL3 has ATP-independent dicing activity and a substrate preference for pre-siRNAs with a 5′-phosphorylated A1 on the Pol IV–produced guide strand and a 1-nt 3′ overhang on the RDR2-produced complementary strand (*22*–*25*).

To analyze 24-nt siRNA production by DCL3, we determined the 3.1-Å-resolution cryo–electron microscopy (cryo-EM) structure of full-length DCL3 in complex with a 40-bp TAS1a-derived pre-siRNA with a 5′-phosphorylated A1 in the guide strand, mimicking the Pol IV strand, and a 1-nt 3′ overhang in the complementary strand, mimicking the RDR2 strand, together with Ca^{2+} ions mimicking Mg^{2+} but preventing dicing (Fig. 1, A and B; fig. S1; and tables S1 and S2). The helicase domain of DCL3 showed faint density and could not be built into the model (Fig. 1B and fig. S1E). Unlike the several reported Dicer structures in the inactive states (*3*, *6*, *7*), our DCL3-RNA structure captured Dicer in a dicing-competent state for the first time. The platform, PAZ, and connector domains form a combined cassette to bind to the RNA duplex end toward the 5′ end of the guide strand and align on one side of the RNA with the RNase IIIa/b domains, forming a continuous positively charged surface to accommodate the RNA (Fig. 1, B to D). On the other side, two dsRNA-binding domains (dsRBDs) interact with the RNA backbone and form an enclosed pre-siRNA–binding channel, enveloping the bound pre-siRNA (Fig. 1, C and D).

Thirty-five base pairs of the pre-siRNA can be traced in the structure and ~33 bp are nearly fully enclosed by DCL3 (Fig. 2A and fig. S2A). The platform, PAZ, and connector domain together accommodate one end of the pre-siRNA (Fig. 2B and fig. S2B), resembling the reported human Dicer platform-PAZ-connector-RNA structure (fig. S2C) (*4*). A PAZ domain loop penetrates the RNA duplex, splitting the first base pair and flipping out the guide strand 5′-phosphorylated A1 into a platform-PAZ-connector pocket, with the orphaned U1′ retaining its original conformation (Fig. 2B). The 5′-phosphate group inserts into a positively charged pocket formed by surrounding basic residues, including Lys695, Lys903, His906, Arg953, and Lys957, to form extensive electrostatic and hydrogen-bonding interactions (Fig. 2C). A sulfate-binding pocket observed in the human Dicer platform-PAZ-connector cassette was proposed to be the 5′-phosphate-binding site (*4*, *5*). Here, our DCL3-RNA complex structure located the 5′-phosphate-binding pocket to a similar position (fig. S2C) and revealed the recognition mechanism, suggesting that Dicer proteins may share the same pocket to recognize the 5′-phosphate group of guide strand RNA.

The flipped-out A1 base is stabilized through stacking interactions with the PAZ domain residue His909 (Fig. 2D), allowing the A1 base to form hydrogen bonds with both the phosphate group of U9′ on the complementary strand and PAZ domain Arg931 (Fig. 2D), explaining the preference of DCL3 for the A1-containing substrate guide strand (*22*–*24*, *26*). Replacement of A1 with other bases revealed that pyrimidines such as U and C are too small to form a similar hydrogen-bonding interaction as adenine (fig. S2D). Although the G base has the potential to form similar hydrogen-bonding interactions (fig. S2D), the three hydrogen bonds of the G-C pair require more energy to disrupt than the two hydrogen bonds of the A-U pair, making base flipping by DCL3 energetically more favorable for A-U than for G-C. Consistent with this reasoning, U is the second most preferred base at guide strand position 1, with C and G not being preferred (*22*). By contrast, DCL4 was reported to have no preference for the 5′-end base of guide strand (*22*), suggesting that different Dicers may use different 5′-end base recognition mechanisms.

The 3′ end of the complementary strand is recognized by a PAZ domain aromatic cap formed by His849, Phe869, Tyr880, Tyr883, Phe884, and Tyr888, which both encloses and provides stacking opportunities with the 3′-end C-1′ base (Fig. 2E and fig. S2B). Additionally, His849, Tyr883, Lys887, and Tyr888 form salt bridge and hydrogen-bonding interactions with the phosphate groups (Fig. 2E).

[1]Key Laboratory of Molecular Design for Plant Cell Factory of Guangdong Higher Education Institutes, Institute of Plant and Food Science, School of Life Science, Department of Biology, Southern University of Science and Technology, Shenzhen, Guangdong 518055, China. [2]Department of Molecular, Cell and Developmental Biology, University of California at Los Angeles, Los Angeles, CA 90095, USA. [3]Ministry of Education Key Laboratory of Protein Science, Tsinghua-Peking Center for Life Sciences, Beijing Advanced Innovation Center for Structural Biology, School of Life Sciences, Tsinghua University, Beijing 100084, China. [4]Department of Plant Sciences, University of Cambridge, Cambridge CB2 3EA, UK. [5]Department of Biochemistry and Molecular Biology, International Cancer Center, Shenzhen University Health Science Center, Shenzhen 518060, China. [6]Howard Hughes Medical Institute, University of California, Los Angeles, CA 90095, USA.
***Corresponding author. Email: dujm@sustech.edu.cn (J.D.); jacobsen@ucla.edu (S.E.J.); liss@szu.edu.cn (S.L.)**
†These authors contributed equally to this work.

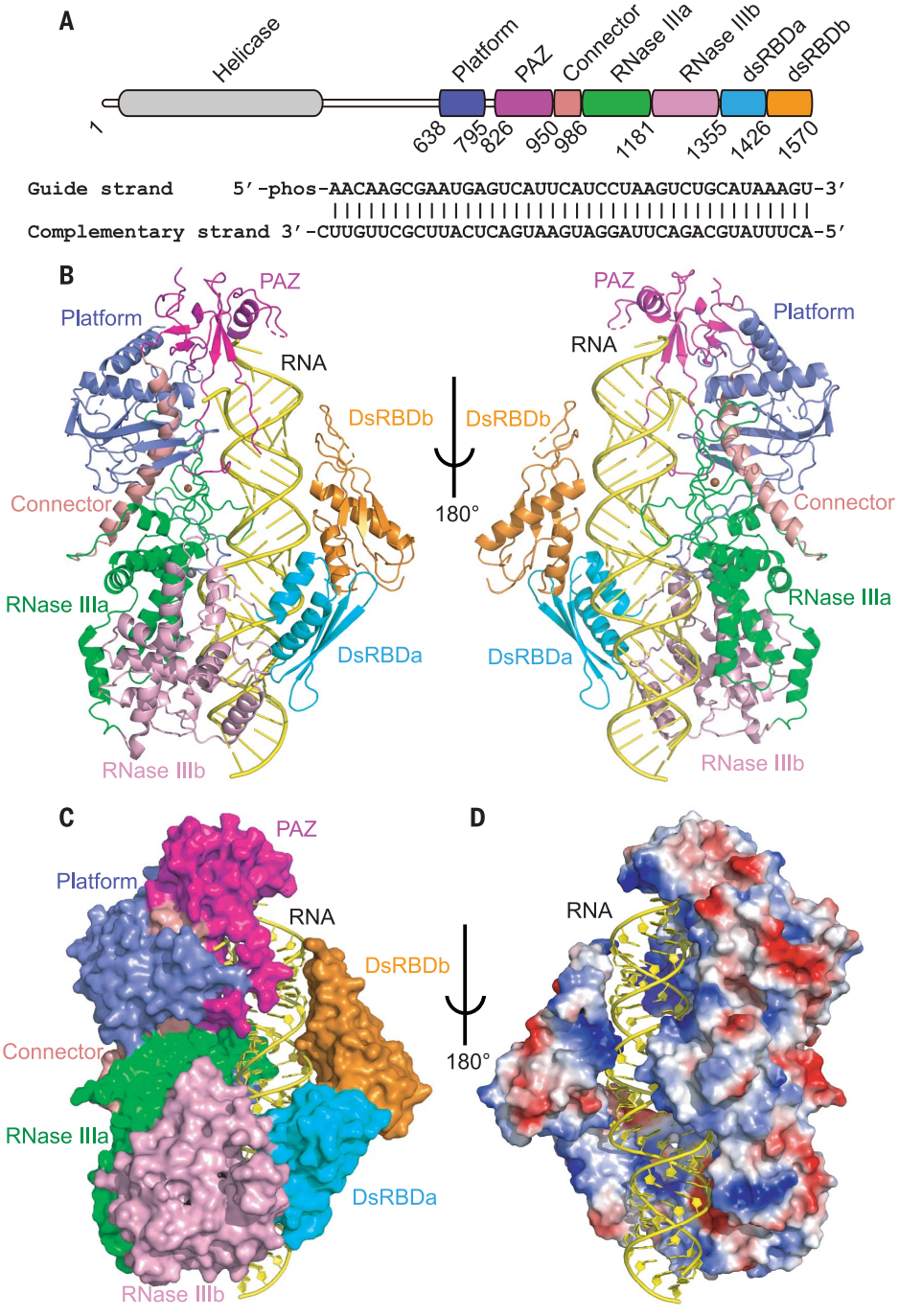

Fig. 1. Structure of *Arabidopsis* DCL3-pre-siRNA complex. (**A**) Domain architecture of *Arabidopsis* DCL3 and sequence of pre-siRNA used for structure determination. (**B**) Overall structure of the DCL3-RNA complex in ribbon representation. (**C**) Structure of DCL3 in surface view and RNA in cartoon view showing the multiple domains of DCL3 wrapping around the RNA. (**D**) Electrostatic surface view of DLC3 showing that the RNA is bound in a positively charged channel. Blue indicates a positively charged region and red a negatively charged region.

Thus, recognition of both the 5′-phosphorylated A1 and the 1-nt 3′ overhang of the bound pre-siRNA duplex by the platform-PAZ-connector cassette supports the previous model that Dicer combines the 5′- and 3′-end recognitions as a start to measure the sRNA length (*3*–*5*).

DCL3 has low but considerable activity toward substrates with 5′-phosphorylated U and/or longer 3′ overhangs (*22*). To understand this binding tolerance, we determined the cryo-EM structure, at 3.73-Å resolution, of DCL3 in complex with a 30-bp pre-siRNA having a guide strand 5′-phosphorylated U1 and a complementary strand 2-nt 3′ overhang (figs. S3 to S4 and tables S1 and S2). The structure closely resembles the DCL3–40-bp RNA complex, with a root mean square difference of 1.9 Å (fig. S4D), but the faint density corresponding to the helicase domain was much weaker and was also not built (fig. S3C). The termini of the RNA can be clearly traced with both bases of the U1-A1′ pair flipped out from the RNA duplex, in contrast to the DCL3-40-bp pre-siRNA complex with only the A1 of guide strand flipped out (Fig. 2, F to H). Recognition of the 5′-phosphorylated U1 in the DCL3-30-bp RNA complex is similar to 5′-phosphorylated A1 in the DCL3-40-bp RNA complex, with the major difference being the lack of a hydrogen bond between the U1 base and the complementary strand (fig. S5A). Superimposition of the dsRNA molecules in the two complexes indicates that the guide strands adopt very similar conformations, whereas the flip out of the complementary strand A1′ of the 2-nt-overhang RNA distorts the backbone of the

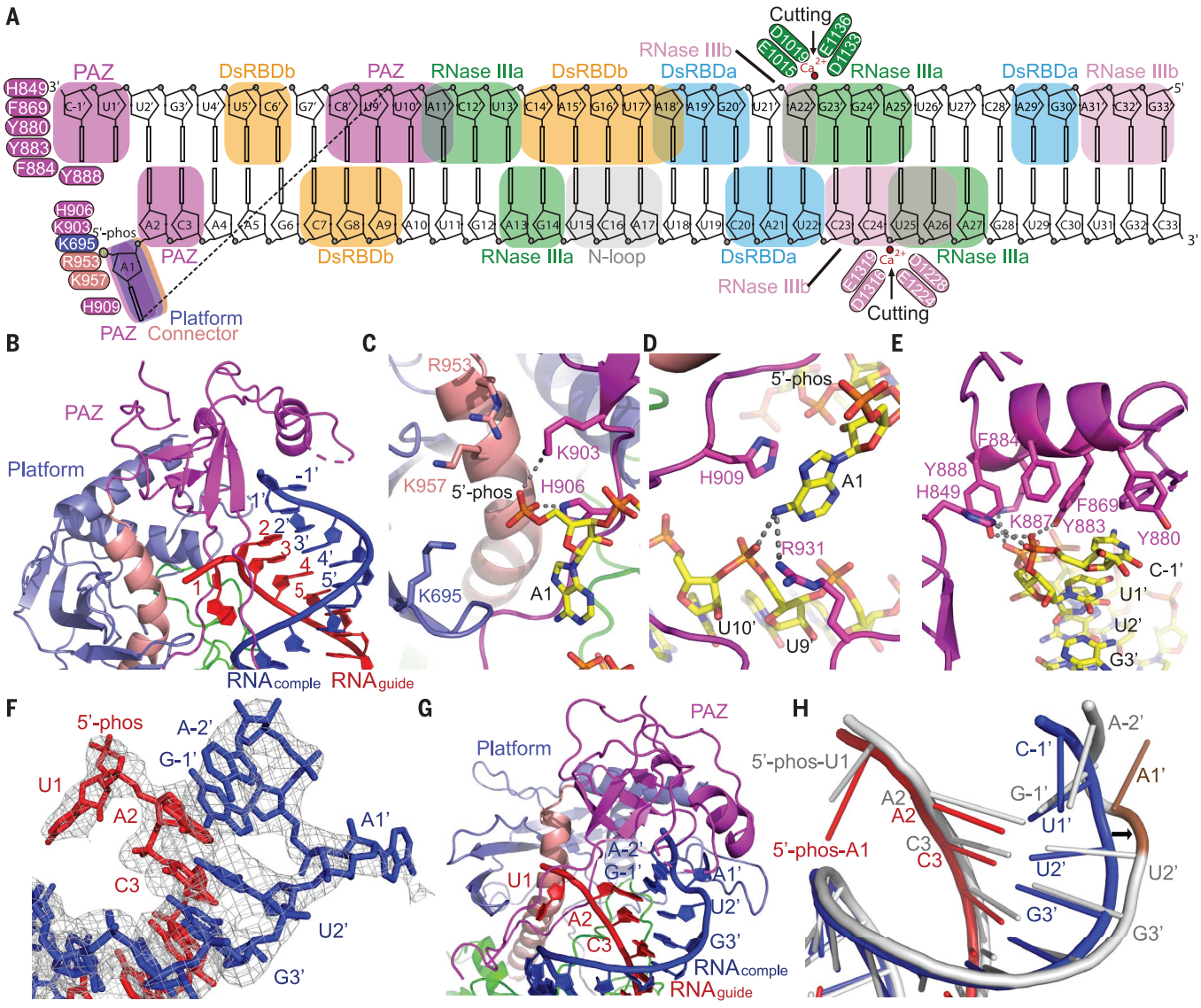

Fig. 2. Terminus-specific recognition of pre-siRNA. (**A**) Schematic representation of the overall interactions between DCL3 and the pre-siRNA. Key residues are highlighted. The RNA-interacting DCL3 domains are indicated by boxes. (**B**) Overall recognition of the RNA termini by the DCL3 platform-PAZ-connector cassette. The guide strand RNA (RNA_{guide}) and complementary strand RNA (RNA_{comple}) are highlighted in red and blue, respectively. (**C**) Recognition of the guide strand 5′-phosphate group by a positively charged pocket in the platform-PAZ-connector cassette. Interacting residues and hydrogen bonds are highlighted in sticks and dashed lines, respectively. (**D**) Specific recognition of the A1 base by stacking with DCL3 H909 and hydrogen-bonding interactions with DCL3 R931 and the complementary strand. (**E**) An aromatic cap covers and interacts with the last base of the 3′ end of the complementary strand. In addition, the phosphate backbone is recognized by hydrogen bonds. (**F**) Termini of the pre-siRNA with 5′-phosphorylated U1 on the guide strand and 2-nt 3′ overhang on the complementary strand. The cryo-EM map is shown in mesh, revealing that both bases of the U1-A1′ pair are flipped out. (**G**) Capturing of the RNA termini with 5′-phosphorylated U1 and the 2-nt 3′ overhang by the platform-PAZ-connector cassette. (**H**) Superimposition of the 1-nt 3′ overhang–containing RNA duplex (in red and blue) and the 2-nt 3′ overhang–containing RNA (in silver). The conformational change of RNA is highlighted by the arrow. The flipped-out A1′ base allows the G-1′ and A-2′ bases to fold back and overlap with positions of U1′ and C-1′ of the 1-nt-overhang RNA occupying the same 3′-end position.

RNA (Fig. 2H and fig. S5B). The overhanging G-1′ and A-2′ turn back, superimposing with the U1′ and C-1′ of the 1-nt-overhang RNA in the DCL3-40-bp RNA complex and are captured by the PAZ domain aromatic cap in a manner similar to the 1-nt-overhang RNA (Fig. 2H and fig. S5C). Because A2 and U2′ are paired in both structures, the longer 3′ overhang can loop out from the 1′ position with the last 2 nt of the overhang folding back and being captured by the PAZ aromatic cap, explaining the tolerance mechanism for the longer 3′ overhang.

Similar to previously reported bacterial or yeast RNase III homodimer structures (*27*, *28*), the two DCL3 RNase III domains adopt a conserved, side-by-side arrangement, with the two corresponding active sites marked by Ca^{2+} ions located at adjacent positions along the two RNA strands flanking the minor groove (Fig. 3A). The RNase IIIa residues Glu1015, Asp1019, Asp1133, and Glu1136 coordinate one Ca^{2+} ion, mimicking the Mg^{2+} ion, to participate in the phosphodiester bond cleavage

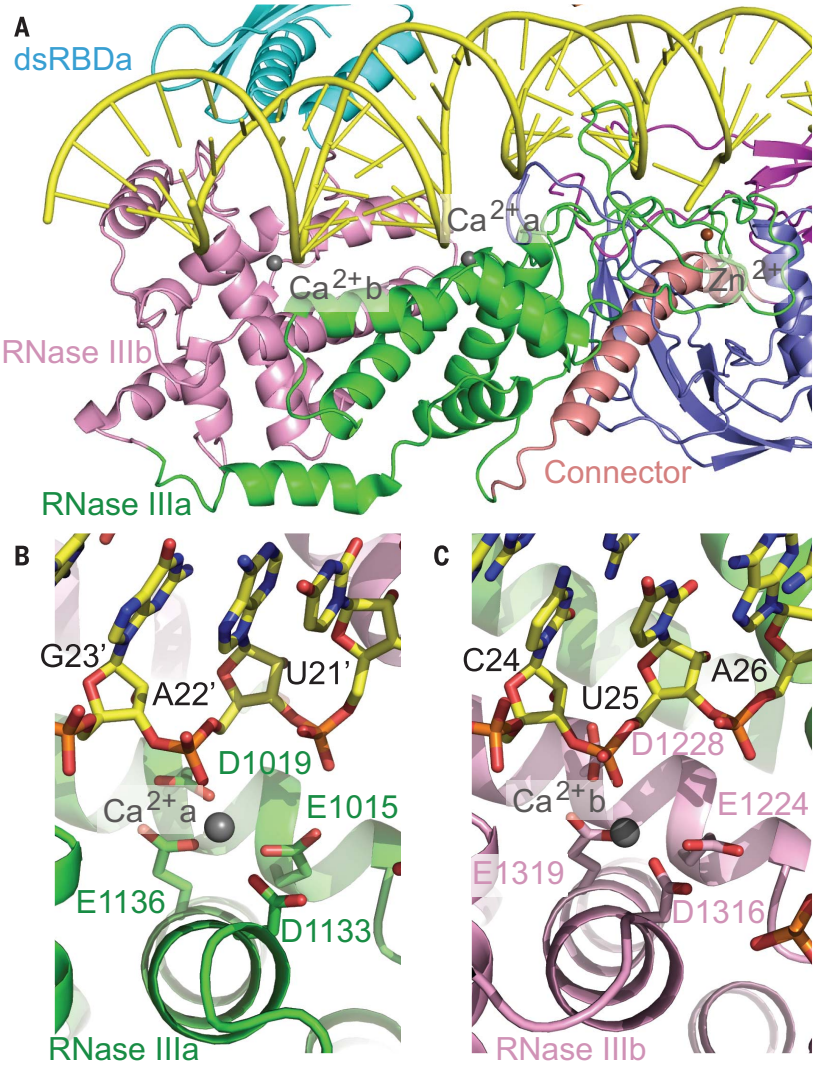

Fig. 3. Active-site conformation. (**A**) Overall structure of the active sites of RNase IIIa and RNase IIIb. (**B** and **C**) Active-site conformation of RNase IIIa (B) and RNase IIIb (C).

between G23′ and A22′ of the complementary strand (Fig. 3B and fig. S2B), producing a 23-nt RNA (C-1′ to A22′). Similarly, the RNase IIIb residues Glu1224, Asp1228, Asp1316, and Glu1319 coordinate a second Ca^{2+} ion to participate in cleavage between C24 and U25 of the guide strand to produce a 24-nt RNA (A1 to C24) (Fig. 3C and fig. S2B). Thus, simultaneous cutting of both strands will produce a dsRNA with newly generated 2-nt 3′ overhang on the guide strand and a 1-nt 3′ overhang on the complementary strand (Fig. 2A), consistent with previous biochemical data (*22*). Consequently, DCL3 mainly produces siRNAs with a 24-nt 5′-phophylated guide strand (Pol IV strand) and a 23-nt 1-nt-overhang complementary strand (RDR2 strand). *In planta*, AGO4 prefers 24-nt siRNAs possessing 5′ A1 as the guide strand (*29*, *30*), perfectly matching the DCL3 Pol IV strand product, which is thus predominately selected by AGO4 to guide RdDM (*23*), resulting in strand-biased 24-nt siRNA production (*23*, *24*).

The two dsRBDs cover the opposite side of pre-siRNA relative to the positions of RNase IIIa/b (Fig. 1C). The two dsRBDs adopt very similar conformations, and their highly positively charged surfaces bind the RNA backbone (fig. S6, A and B). Although both the 5′ half (A2 to U18) and the 3′ half (C23 to C33) of the pre-siRNA adopt A-form conformations, the two segments do not align because of a conformational distortion in the central region (U19 to U22) (fig. S6C), which can also be observed in the DCL3–30-bp RNA complex (fig. S6D). This conformational change displaces the 3′ half of the RNA toward the DCL3 active sites (fig. S6E). In the substrate-loaded yeast RNase III Rnt1p-RNA complex structure, although the Rnt1p-RNase III homodimer is well superimposed with the RNase IIIa/b of DCL3, the two RNA molecules bounded by Rnt1p homodimer mimic the 5′ half and 3′ half of the DCL3-bound RNA, respectively, shifting at the same position corresponding to U19 to U22 of DCL3-complexed RNA (fig. S6E) (*27*). By contrast, the two dsRBDs of the Rnt1p homodimer occupy positions other than the dsRBDa/b of DCL3 (fig. S6E) (*27*). Together, the similar RNA conformational change upon binding by RNase IIIs and the different dsRBD-binding positions along the RNA suggest a plausible dynamic active dicing model in which the RNase IIIs capture and twist the RNA, whereas the dsRBDs dynamically bind at different positions during the dicing process. Because of the limited available structures, more Dicer-RNA complex structures in different states are required to shape the precise overall working model for Dicer.

We performed structure-based mutagenesis studies both in vitro and in vivo. Wild-type (WT) DCL3 cuts a 30-bp pre-siRNA with a 5′-phosphorylated A1 and a 1-nt 3′ overhang into 24- and 23-nt bands efficiently (Fig. 4, A and B). Mutations in the 5-phosphate-binding pocket (K695A/K957A/K903A), A1 recognition (H909A), and 3′-binding PAZ domain aromatic cap (Δ865-895) all showed decreased activity compared with WT (Fig. 4A and fig. S7A), indicating the role of both 5′ and 3′ counting in dicing. Both the dsRBDb deletion (Δ1450 to 1570) and the dsRBDa/b deletion construct (Δ1356 to 1570) decreased DCL3 activity, suggesting that the dsRBDs contribute to enzymatic processing (Fig. 4A and fig. S7A). An RNase IIIa active-site mutant (E1015A/D1019A/D1133A/E1136A) generated only 24-nt sRNAs and no 23-nt sRNAs (Fig. 4B), whereas an RNase IIIb mutant (E1224A/E1228A/D1316/E1319A) generated only 23-nt sRNAs and no 24-nt sRNAs (Fig. 4B), confirming that RNase IIIa and RNase IIIb are responsible for complementary strand and guide strand cleavage, respectively.

To further understand the influence of the 3′ overhang, we tested RNA substrates with the same 5′-phosphorylated A1 in the guide strand but with various 3′ overhangs in the complementary strand. Consistent with our structural observations, longer 3′ overhangs decreased activity (Fig. 4C and fig. S7B). Moreover, these dsRNAs were cut into one consensus 24-nt band and the other bands ranged from 23 to 26 nt, depending on overhang lengths (fig. S7B), suggesting that 5′ counting predominates over 3′ counting. Thus, the sRNA-counting mechanism of DCL3 appears to rely more on measurement of the guide strand RNA length through the recognition of the 5′ phosphate and flipped-out base by the platform-PAZ-connector cassette and Mg^{2+}-mediated RNA cleavage by the RNase

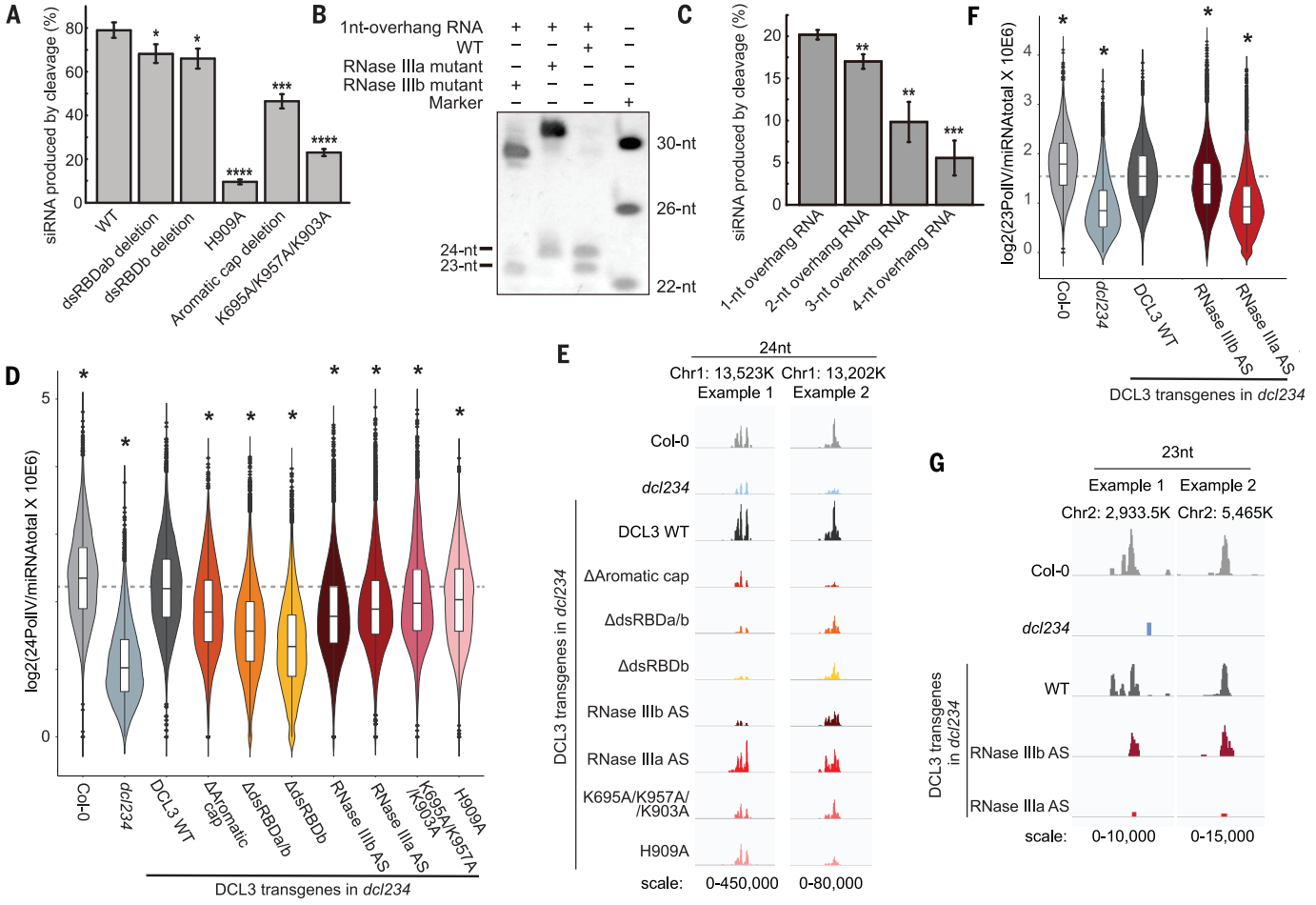

Fig. 4. Biochemical and in vivo assays. (**A**) In vitro dicing of DCL3 and its mutants. Aromatic cap deletion, Δ865-895; dsRBDb deletion, Δ1450-1570; dsRBDa/b deletion, Δ1356-1570. (**B**) In vitro dicing of DCL3 WT, RNase IIIa mutants (D1133A/E1136A/E1015A/D1019A), and RNase IIIb mutants (D1316A/E1319A/E1224A/D1228A). (**C**) DCL3 dicing activity against different RNAs with the same guide strand having 5′-phophorylated-A1 and different complementary strands, with the 3′ overhang ranging from one to four nucleotides. The in vitro assays were performed in a 50-μl reaction system containing 0.003 nmol [(A) and (C)] or 0.024 nmol (B) DCL3 or its mutants and 0.01 nmol substrate RNA at 37°C. The reaction times were set to 5 min (A), 40 min (B), and 2 min (C). In (A) and (C), the percentages of the product siRNA are shown as means ± SD (n = 3); two-tailed Student's t test was applied: *P < 0.05, **P < 0.01, ***P < 0.001, and ****P < 0.0001. (**D** and **F**) Violin plot showing the abundance of 24-nt (D) and 23-nt (F) sRNAs over Pol IV–dependent sRNA regions normalized to total miRNAs (n = 7632). Data represent the average of two biological replicates from two independent T_1 plants. Two-tailed Student's t test was used to determine the significance of difference for each indicated genotype compared with the DCL3 WT complementing line. *P < 0.01. AS, active-site mutant. (**E** and **G**) Screen shots showing the abundance of 24-nt (E) and 23-nt (G) sRNAs over two example regions.

IIIb domain. By contrast, the *Giardia* Dicer was reported to strictly obey the 3′-counting rule (*3*, *5*), suggesting that different Dicers have different counting-end preferences.

To assess the in vivo functions of DCL3, WT pDCL3::DCL3-3xFLAG (hereafter DCL3 WT) or various mutants were transformed into the *Arabidopsis dcl2 dcl3 dcl4* (*dcl234*) triple-mutant background to avoid potential complications caused by the partial functional redundancy with DCL2/4 (*9*, *16*) (fig. S8). The abundance of 24-nt sRNAs over Pol IV regions (*23*) was examined in two independent T_1 plants of each genotype. DCL3 WT restored the biogenesis of 24-nt sRNAs to near WT levels when transformed into *dcl234* (Fig. 4, D to E). Consistent with the in vitro studies, the 5′-binding mutants (K695A/K957A/K903A to reduce 5′-phosphate binding and H909A to reduce 5′-A1 base recognition) and the 3′-binding mutant (Δ865-895 to delete the aromatic cap) all led to significant losses of 24-nt sRNA (Fig. 4, D to E). Deletions of dsRBDa/b (Δ1356 to 1570) or dsRBDb (Δ1450 to 1570) both failed to restore 24-nt sRNA generation (Fig. 4, D to E). The D1316A/E1319A/E1224A/D1228A mutant, which disrupts RNase IIIb and guide strand processing, led to a significant loss of 24-nt siRNA in vivo (Fig. 4, D to E). The D1133A/E1136A/E1015A/D1019A mutant, which affects RNase IIIa and complementary strand processing, led to a strong loss of 23-nt siRNA in vivo (Fig. 4, F to G). We observed a moderate loss of 23-nt sRNAs in the RNase IIIb mutant and a mild loss of 24-nt sRNAs in the RNase IIIa mutant (Fig. 4, D to G). These observations likely indicate that the stabilities of 23- and 24-nt sRNA are dependent on each other. This stability interdependence may take place before the 24-nt sRNAs are loaded onto AGO4, or the 23-nt passenger strand may facilitate the loading of the 24-nt sRNA onto AGO4 and thus lead to its stabilization. An equally plausible explanation is that cleavage of the two strands is coupled in vivo. Further experimental evidence is required to shed light on these hypotheses.

We further compared DCL3 with human and *Giardia* Dicers. Although the RNase IIIa/b active sites are conserved, the platform-PAZ-connector cassette of human Dicer is positioned closer to the RNA termini (fig. S9A), whereas

in *Giardia* Dicer, the platform-PAZ-connector cassette is positioned farther away from the RNA termini, allowing the binding of longer RNAs (fig. S9B), consistent with the human and *Giardia* Dicers producing slightly shorter (22-nt) or longer (25-nt) sRNAs, respectively, than DCL3 (*3*, *6*). Thus, the sRNA product length of different Dicers likely depends on the relative orientation and/or positioning between the RNase IIIa/b active sites and platform-PAZ-connector cassettes. Considering that the human and *Giardia* Dicer structures are not in the dicing-competent conformation, it is also possible that they may take conformational change in active dicing. Future work on more cleavage-competent conformation Dicer structures is required to fully reveal the product length determination mechanism of Dicer proteins.

In conclusion, the DCL3-RNA complex structures in dicing-competent states reveal the molecular basis for the terminus specificity, accurate length measurement, and the strand-biased 24-nt siRNA production by DCL3. Given the overall shared length measurement and dicing mechanism of Dicers, our structure also provides insight into the general principle of length measurement and asymmetric cutting by Dicers from other species, which may allow us to design engineered Dicers to produce sRNAs with defined terminus preferences and lengths.

REFERENCES AND NOTES

1. V. N. Kim, J. Han, M. C. Siomi, *Nat. Rev. Mol. Cell Biol.* **10**, 126–139 (2009).
2. G. Meister, *Nat. Rev. Genet.* **14**, 447–459 (2013).
3. I. J. Macrae *et al.*, *Science* **311**, 195–198 (2006).
4. Y. Tian *et al.*, *Mol. Cell* **53**, 606–616 (2014).
5. J. E. Park *et al.*, *Nature* **475**, 201–205 (2011).
6. Z. Liu *et al.*, *Cell* **173**, 1191–1203.e12 (2018).
7. N. K. Sinha, J. Iwasa, P. S. Shen, B. L. Bass, *Science* **359**, 329–334 (2018).
8. X. Song, Y. Li, X. Cao, Y. Qi, *Annu. Rev. Plant Biol.* **70**, 489–525 (2019).
9. I. R. Henderson *et al.*, *Nat. Genet.* **38**, 721–725 (2006).
10. Z. Xie, E. Allen, A. Wilken, J. C. Carrington, *Proc. Natl. Acad. Sci. U.S.A.* **102**, 12984–12989 (2005).
11. A. Deleris *et al.*, *Science* **313**, 68–71 (2006).
12. H. Wu *et al.*, *Nature* **581**, 89–93 (2020).
13. R. A. Mosher, F. Schwach, D. Studholme, D. C. Baulcombe, *Proc. Natl. Acad. Sci. U.S.A.* **105**, 3145–3150 (2008).
14. M. Ronemus, M. W. Vaughn, R. A. Martienssen, *Plant Cell* **18**, 1559–1574 (2006).
15. F. Vazquez *et al.*, *Mol. Cell* **16**, 69–79 (2004).
16. Z. Xie *et al.*, *PLOS Biol.* **2**, E104 (2004).
17. X. Zhang, I. R. Henderson, C. Lu, P. J. Green, S. E. Jacobsen, *Proc. Natl. Acad. Sci. U.S.A.* **104**, 4536–4541 (2007).
18. X. Cao, S. E. Jacobsen, *Curr. Biol.* **12**, 1138–1144 (2002).
19. C. F. Li *et al.*, *Cell* **126**, 93–106 (2006).
20. A. T. Wierzbicki, T. S. Ream, J. R. Haag, C. S. Pikaard, *Nat. Genet.* **41**, 630–634 (2009).
21. D. Zilberman, X. Cao, S. E. Jacobsen, *Science* **299**, 716–719 (2003).
22. H. Nagano, A. Fukudome, A. Hiraguri, H. Moriyama, T. Fukuhara, *Nucleic Acids Res.* **42**, 1845–1856 (2014).
23. J. Zhai *et al.*, *Cell* **163**, 445–455 (2015).
24. J. Singh, V. Mishra, F. Wang, H. Y. Huang, C. S. Pikaard, *Mol. Cell* **75**, 576–589.e5 (2019).
25. Y. Qi, A. M. Denli, G. J. Hannon, *Mol. Cell* **19**, 421–428 (2005).
26. S. Li *et al.*, *Genome Res.* **25**, 235–245 (2015).
27. H. Song *et al.*, *Structure* **25**, 353–363 (2017).
28. J. Gan *et al.*, *Cell* **124**, 355–366 (2006).
29. S. Mi *et al.*, *Cell* **133**, 116–127 (2008).
30. Y. Qi *et al.*, *Nature* **443**, 1008–1012 (2006).

ACKNOWLEDGMENTS

We thank the staff at SUSTech Cryo-EM Center for assistance during data collection, D. Patel for critical reading, and G. Riddihough (LSE) for editing. **Funding:** This work was supported by the National Key R&D Program (2016YFA0503200), the Shenzhen Science and Technology Program (JCYJ20200109110403829 and KQTD20190929173906742), SUSTech (G02226301), the Key Laboratory of Molecular Design for Plant Cell Factory of Guangdong Higher Education Institutes (2019KSYS006 to J.D.), the Guangdong Innovation Research Team Fund (2016ZT06S172 to S.L.), and the National Institutes of Health (R35GM130272 to S.E.J.). S.E.J. is an investigator at the Howard Hughes Medical Institute. **Author contributions:** Q.W., C.W., L.X., and Z.Y. performed the biochemical and structural experiments. Y.X., Z.Z., S.F., and C.H. performed the functional experiments. L.Z. contributed to the cryo-EM data processing. Z.W., J.Z., and M.Y. provided helpful discussions. S.L. directed the in vitro assay. S.L., S.E.J., and J.D. supervised the project and wrote the manuscript. **Competing interests:** The authors declare no competing interests. **Data and materials availability:** Cryo-EM maps have been deposited in the Electron Microscopy Data Bank (EMDB) with accession codes EMD-31963 and EMD-31964. The structures have been deposited in the Protein Data Bank with accession codes 7VG2 and 7VG3. Small RNA sequencing data are accessible at the National Center for Biotechnology Information's Gene Expression Omnibus (GEO) with accession code GSE179616.

SUPPLEMENTARY MATERIALS

science.org/doi/10.1126/science.abl4546
Materials and Methods
Figs. S1 to S9
Tables S1 to S2
References (*31*–*45*)
MDAR Reproducibility Checklist

View/request a protocol for this paper from *Bio-protocol*.

14 July 2021; accepted 1 October 2021
Published online 14 October 2021
10.1126/science.abl4546

Science

Mechanism of siRNA production by a plant Dicer-RNA complex in dicing-competent conformation

Qian WangYan XueLaixing ZhangZhenhui ZhongSuhua FengChangshi WangLifan XiaoZhenlin YangC. Jake HarrisZhe WuJixian ZhaiMaojun YangSisi LiSteven E. JacobsenJiamu Du

Science, 374 (6571), • DOI: 10.1126/science.abl4546

Ready to dice

In the biogenesis of small RNAs, the Dicer family endonucleases act as a molecular ruler to cut the substrate RNA into defined lengths. Wang *et al*. report a structure of the dicing-competent state of plant DICER LIKE PROTEIN 3 (DCL3) in complex with a pre–small interfering RNA (pre-siRNA). Toward one end of the pre-siRNA, DCL3 uses a positively charged pocket and an aromatic cap to specifically recognize the 5#-phosphorylated adenosine of the guide strand and the 3# overhang of the complementary strand, respectively. On the other end, the paired ribonuclease III domains of DCL3 cut both strands of the RNA, determining the precise length of the product small RNA. —DJ

Science (ISSN) is published by the American Association for the Advancement of Science. 1200 New York Avenue NW, Washington, DC 20005. The title *Science* is a registered trademark of AAAS.